Structure

α- and β-Tubulin Lattice of the Axonemal Microtubule Doublet and Binding Proteins Revealed by Single Particle Cryo-Electron Microscopy and Tomography

Graphical Abstract

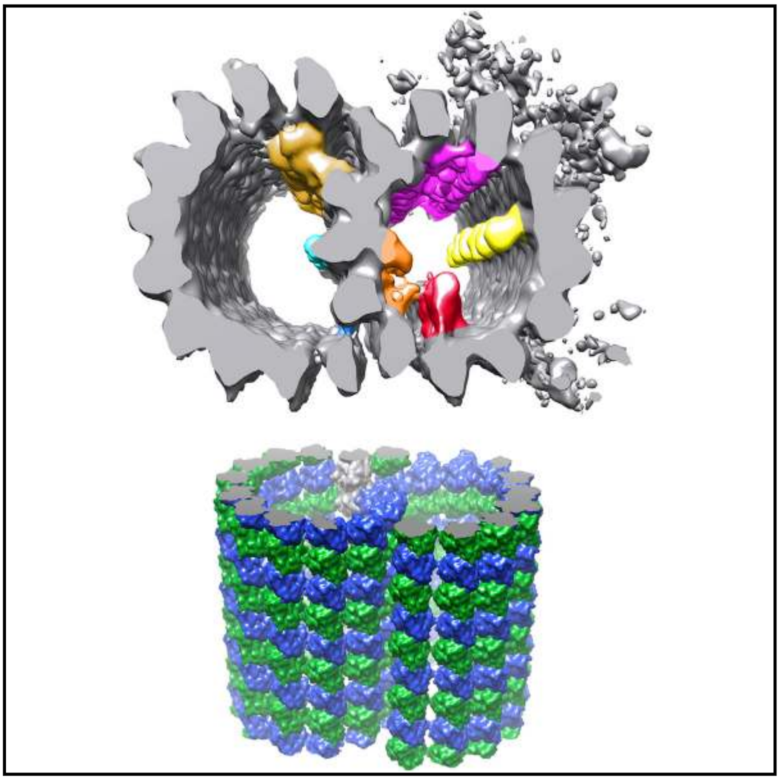

Authors

Aditi Maheshwari, Jagan Mohan Obbineni, Khanh Huy Bui, Keitaro Shibata, Yoko Y. Toyoshima, Takashi Ishikawa

Correspondence

takashi.ishikawa@psi.ch

In Brief

Single particle cryo-EM allowed Maheshwari et al. to reconstruct the detailed structure of ciliary MTD, which was not visualized by cryo-electron tomography. The A and B tubules are in the B-lattice form with the seam at the external junction of the A tubule. Inner dynein tails and internal proteins form inter-protofilament connections.

Highlights

- Single particle cryo-EM visualized ciliary MTD at unprecedented resolution
- Both A and B tubules of ciliary MTD take B lattice
- The lattice seam is located at the outer junction
- MIPs and inner dyneins form inter-protofilament connections

Accession Numbers

3JAO

Maheshwari et al., 2015, Structure *23*, 1584–1595
September 1, 2015
http://dx.doi.org/10.1016/j.str.2015.06.017

Structure
Article

α- and β-Tubulin Lattice of the Axonemal Microtubule Doublet and Binding Proteins Revealed by Single Particle Cryo-Electron Microscopy and Tomography

Aditi Maheshwari,[1,2] Jagan Mohan Obbineni,[1] Khanh Huy Bui,[1,4] Keitaro Shibata,[3] Yoko Y. Toyoshima,[3]
and Takashi Ishikawa[1,*]
[1]Biomolecular Research Laboratory, Paul Scherrer Institute, 5232 Villigen PSI, Switzerland
[2]Department of Biology, ETH Zurich, Otto-Stern-Weg 5, 8093 Zurich, Switzerland
[3]Department of Life Science, Graduate School of Arts and Sciences, University of Tokyo, 3-8-1 Komaba, Meguro-ku, Tokyo 153-8902, Japan
[4]Present address: Department of Anatomy and Cell Biology, McGill University, Canada
*Correspondence: takashi.ishikawa@psi.ch
http://dx.doi.org/10.1016/j.str.2015.06.017

SUMMARY

Microtubule doublet (MTD) is the main skeleton of cilia/flagella. Many proteins, such as dyneins and radial spokes, bind to MTD, and generate or regulate force. While the structure of the reconstituted microtubule has been solved at atomic resolution, nature of the axonemal MTD is still unclear. There are a few hypotheses of the lattice arrangement of its α- and β-tubulins, but it has not been described how dyneins and radial spokes bind to MTD. In this study, we analyzed the three-dimensional structure of *Tetrahymena* MTD at ~19 Å resolution by single particle cryo-electron microscopy. To identify α- and β-tubulins, we combined image analysis of MTD with specific kinesin decoration. This work reveals that α- and β-tubulins form a B-lattice arrangement in the entire MTD with a seam at the outer junction. We revealed the unique way in which inner arm dyneins, radial spokes, and proteins inside MTD bind and bridge protofilaments.

INTRODUCTION

Microtubule doublets (MTDs) are highly conserved structural components of the axoneme that usually form arrays of nine MTDs arranged around two singlet microtubules (MTs) (9 + 2 structure) and consist of more than 400 proteins (Pazour et al., 2005). Only a few are relatively well described regarding the architecture in the axoneme and their functions: inner and outer dyneins are ATP-driven motors, connecting between two adjacent MTDs, and radial spokes (RSs) are T-shaped protein complexes protruding from MTD toward the central pair microtubule singlet. Many other unidentified proteins in flagella/cilia are believed to bind to MTD. Each MTD is made up of a complete tubule (the A tubule) with 13 protofilaments (PFs), and an incomplete tubule (the B tubule) with probably 10 PFs. The PFs themselves are made up of tubulin heterodimers consisting of α- and β-tubulins, similar to the singlet microtubule. Despite recent progress in our knowledge about axonemal structures, mainly revealed by cryo-electron tomography (cryo-ET), the detailed 3D structure of MTD and the molecular arrangement of tubulins within it have never been reported, due to lack of resolution.

The differences between α- and β-tubulin are subtle. Guanosine triphosphate binds to both the tubulins, but is hydrolyzed only on β-tubulin. On the other hand, Taxol binds only to β-tubulin. Some post-translational modifications targeting the C terminus are specific to α-tubulin (Konno et al., 2012). The M loop (amino acids [aa] 272–286 in the case of pig tubulin), which participates in the lateral binding with the neighboring PF, has a difference in conformation for both the tubulins (Nogales et al., 1998). The stabilizing loop (aa 356–372 in the case of pig α-tubulin), which corresponds to the Taxol-binding site in the β-tubulin, is longer in α-tubulin than in β-tubulin (Amos and Löwe, 1999; Nogales et al., 1998).

Axonemal MTDs from cilia/flagella have a complex structure. It has been shown that each MTD is decorated with outer dynein arms (ODAs), inner dynein arms (IDAs), radial spokes (RSs), and dyneins regulatory complexes (DRC/nexin) with periodicities of 24 nm (ODA) and 96 nm (IDA, RS, DRC/nexin) (Goodenough and Heuser, 1985a, 1985b; Porter, 1996). More recently, cryo-ET has revealed 3D structures of the axoneme at ~30 Å resolution (Bui et al., 2008, 2009, 2012; Heuser et al., 2009; Movassagh et al., 2010; Pigino et al., 2011). Cryo-ET described the arrangement and the conformation of ODA, IDA, RS, and DRC/nexin, and revealed components associated with the inside of the MTDs of *Chlamydomonas reinhardtii*, *Tetrahymena thermophila*, and sea urchin sperm (Nicastro et al., 2006, 2011; Pigino et al., 2012; Sui and Downing, 2006), which are now referred to as microtubule inner proteins (MIPs). While flagella of protists (e.g. *Chlamydomonas*) and metazoans (e.g. sea urchin) share a similar arrangement of MIPs, their composition and functions are unknown.

Although the arrangement of these various external and internal MTD-binding proteins were studied by cryo-ET(Bui et al., 2009, 2012; Heuser et al., 2012; Nicastro et al., 2011; Pigino et al., 2011, 2012), the interfaces between these binding proteins and tubulins are unknown. This is mainly because the cryo-ET studies have not reached sufficient resolution to resolve α- and β-tubulin subunits and distinguish between α- and β-tubulins. To study the interface, we first have to locate tubulin subunits in MTD and identify the lattice pattern of tubulin isoforms to reveal their lattice arrangement in MTD. Amos and Klug (1974) pioneered the study on the arrangement of tubulin and proposed different lattice types for the A and B tubules of the MTD, called the A and B lattice, respectively. The A lattice is defined by a left-handed helical arrangement of the PFs with a 4.9-nm stagger between α-α and β-β tubulins from adjacent PFs, whereas the B lattice is defined by a 0.92-nm stagger (12 nm/13 for a three-start helix with 4 nm periodicity and 13 PFs). A three-start helix with13-PF microtubule in B lattice will result in a discontinuity called a seam (Kikkawa et al., 1994). On the other hand, based on the diffraction study of MTD with kinesin binding, Song and Mandelkow (1995) proposed that both tubules follow the B-lattice type. However, both of these studies were based only on 2D diffraction from electron micrographs of negatively stained MTDs. A 3D reconstruction with clear identification of tubulin isoforms can resolve this controversy and help locate the seam in the case of the B lattice. Other proteins that bind to cytoplasmic microtubules, such as kinesin (Cochran et al., 2009; Sindelar and Downing, 2010), the MT-binding domain (MTBD) of dynein (Redwine et al., 2012), and EB1 (Maurer et al., 2012), were studied in detail by cryo-electron microscopy (cryo-EM) at a resolution allowing tubulin isoforms to be identified. These studies achieved higher resolution using a reconstituted system by single particle analysis. Unfortunately, MTD has never been reconstituted in vitro as it is a complex structure. For this case, alternative techniques are needed to achieve 3D structural analysis at higher resolution to allow an understanding of how dynein tails, RSs, MIPs, and other binding proteins interact with MTD.

The manner in which these external and luminal proteins bind is intriguing: do they bind to the α- or β-tubulin? Do they bind in the midst of the PF or between PFs? Do tails of inner dynein isoforms bind to the MTD in the same way as the MTBD? Do all three RSs have the same pattern of interactions with the PFs? Answers to these questions can be found by analyzing the lattice arrangement of α- and β-tubulins in flagellar MTDs and the binding of other proteins on MTD. Identification of tubulin isoforms in situ has not been possible by the previous approach of using cryo-ET of the intact axoneme. Therefore, either a high-resolution MTD structure or decoration specific to a tubulin isoform is needed.

In this study, we analyzed the 3D structure of MTD at unprecedented resolution using the single particle analysis cryo-EM technique. Furthermore, by utilizing β-tubulin-specific kinesin decoration to MTD, we identified the pattern of tubulin isoforms. Thus, we revealed the lattice arrangement and the manner in which ODAs, IDAs, RSs, and MIPs bind to the tubulin backbone. We discuss these new findings in terms of structure and possible function.

RESULTS

Single Particle Analysis of MTD Split from the Axoneme

The 3D structure of the MTD was reconstructed from 10,700 segments of 96-nm length, windowed from electron micrographs of MTDs obtained by treating axonemes of *T. thermophila* with salt and ATP (Figure S1C). Using the technique of single particle analysis, the resolution evaluated by gold standard refinement Fourier shell correlation (FSC) at 0.143 criterion (Rosenthal and Henderson, 2003) was 23 Å, higher than any previous structural analysis of MTDs reconstructed by cryo-ET (Figure 1). The high-resolution structure demonstrated a distortion in the A tubule as reported in the previous studies performed using cryo-ET of intact axonemes (Bui et al., 2012) and split axonemes (Sui and Downing, 2006). The distortion was ~20% as measured by placing the long axis of an ellipse between PFs A2 and A9. In terms of the number of PFs, the A tubule is similar to a 13-PF microtubule. However, it is elongated in the direction of PF-A8/A9 and PF-A2/A3 (Figure 2A). Here, we followed the numbering of Linck and Stephens (2007), which is different from the numbering in our previous work and Sui and Downing (2006). For a more detailed insight into the PF numbering and the corresponding differences, refer to Linck and Stephens (2007). In the reconstituted microtubules the rise (stagger) of subunits from one PF to the next is always uniform (0.9 nm), whereas in the MTD it varies. The stagger of the subunits in the area between the outer and inner junctions of A and B tubules, called the ribbon region, is smaller when compared with the rest of the A tubule, as shown in Figure 2E. These distortions might be due to the binding of inner and outer proteins.

In this reconstruction, the density of each tubulin subunit is distinguishable, enabling us to fit atomic models. On further extracting and averaging cubes of 16-nm edge lengths from the 96-nm repeating unit, the resolution (FSC = 0.143) was improved to 19 Å (24 Å at FSC = 0.5). This unprecedented resolution was due to lower total radiation damage, contrast transfer function (CTF) correction during single particle analysis, and thinner vitreous ice compared with the intact flagellum. The current resolution is sufficient to resolve each PF of both A and B tubules as well as tubulin subunits, which was not clear by cryo-ET (compare Figures 1A, 1D, and 1G and Figures 1B, 1E, and 1H, respectively). The electron density for MIPs appears more defined than that obtained by cryo-ET (Linck et al., 2014; Nicastro et al., 2011; Pigino et al., 2012; Sui and Downing, 2006) (details discussed in the section on Microtubule Inner Proteins). However, it is not possible to directly distinguish α- and β-tubulin by eye. Therefore, we decorated MTDs with kinesin heads (rk354) and did computational cross-correlation coefficient (CCC) analysis to assign tubulin isoforms to characterize the lattice patterns in the A and B tubules (discussed in the next two sections).

The 19-Å map highlights similarity and difference between PFs from MTD and in vitro reconstituted pure MT (Alushin et al., 2014) (PDB: 3J6F). In the 19-Å density map, computed by low-pass filtering the atomic models (Figure 2C), there is a difference in density between the intra-dimer interface (i.e. the interface between α-tubulin and the distal β-tubulin within the same tubulin heterodimer) and the inter-dimer interface (i.e. the interface between β-tubulin and the α-tubulin of the next distal tubulin heterodimer); density is higher at the intra-dimer interface than at the inter-dimer interface. Similar phenomena were found in the map of MTD, in many PFs (PF-A2–A6, A11–A13; PF-B1–B6, B8–B10); a subunit is connected to an adjacent subunit with higher density than to the other adjacent subunit (shown in grayscale gradient and contour maps, on the right in each panel of Figure 2B and Figure S2). The adjacent subunits are connected at the area close to the external surface of the microtubule.

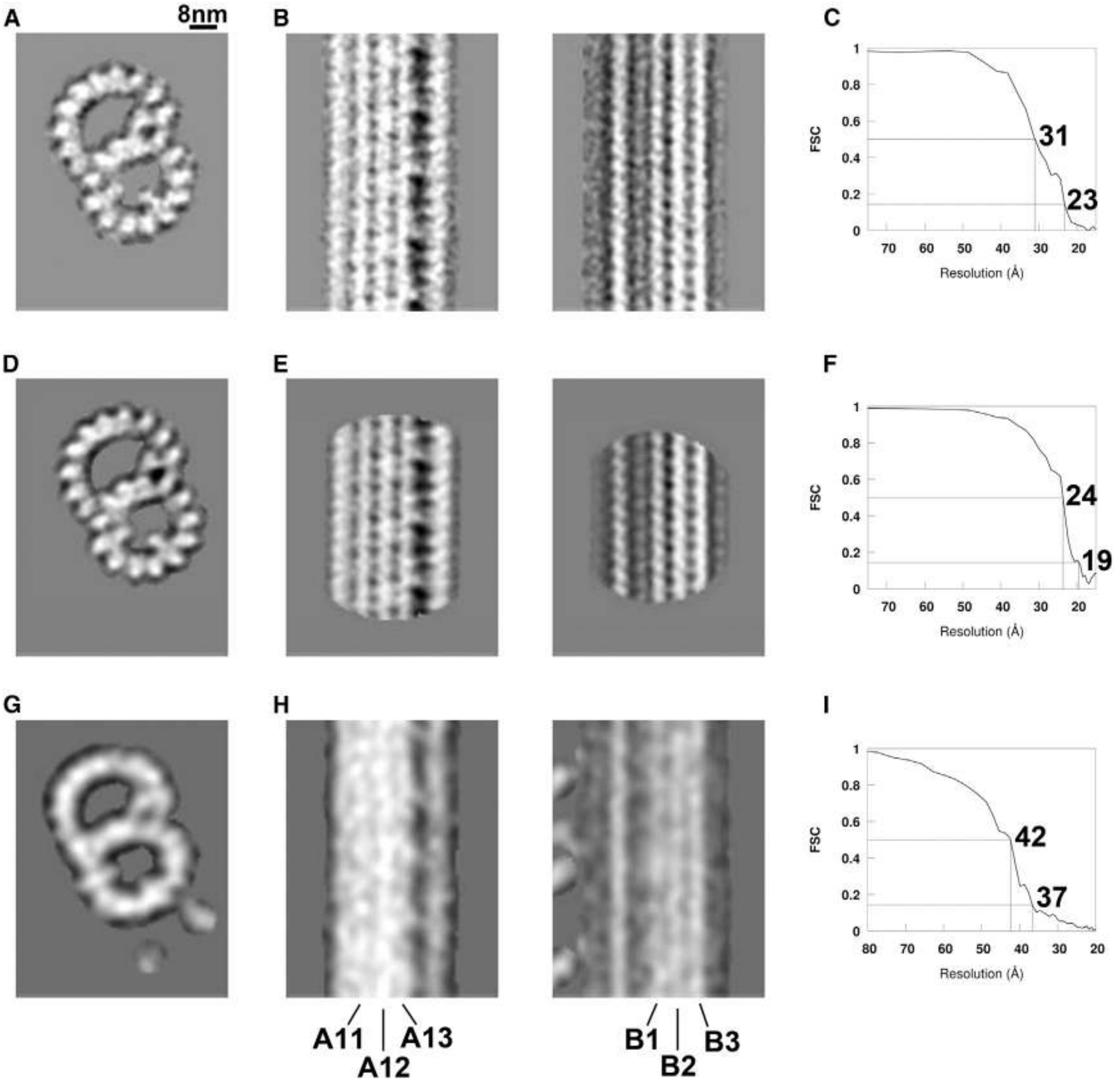

Figure 1. Comparison of Axonemal Microtubule Doublet Structure from Cryo-Single Particle Analysis and Cryo-ET

(A–F) Single particle analysis.

(G–I) Cryo-ET (Pigino et al., 2012).

(A, D, G) Cross section of the axonemal doublet (seen from the distal [+] end). (B, E, H) Longitudinal sections of PFs of the A and B tubules at the same position on the microtubule doublet structure (MTD) (top: distal [+] end; bottom: proximal [−] end). (C, F, I) The FSC curve showing the resolution. 23 Å with gold standard refinement FSC = 0.143 (31 Å at FSC = 0.5) and 19 Å (24 Å with FSC = 0.5) resolutions were achieved with single particle analysis (A–C) and further averaging with 16-nm periodicity (D–F), respectively. The PFs are well resolved and the tubulin subunits can be clearly distinguished. At the 37-Å resolution attained with cryo-ET, a good resolution for this technique, the PFs are not well resolved.

The scale bar in (A) indicates 8 nm and is applicable to all panels. The PF numbers are indicated in (H).

Assignment of α- and β-Tubulin Subunits by Kinesin Decoration

The lattice arrangement for the A and B tubules of the MTD has long been debated since the pioneer work of Amos and Klug in the 1970s (Amos and Klug, 1974; Song and Mandelkow, 1995). The tubulin isoforms have never been identified for each PF of the MTD in 3D reconstruction maps. We attempted to identify tubulin isoforms using cryo-ET of kinesin-decorated MTD, and computational fitting of atomic models to single particle analysis. Fitting between single particle analysis and tomography is based on CCC and obviously proved by matching of MIPs (arrowheads in Figures 2B and S2 and Video S1). Since kinesin is known to bind to β-tubulin (Song and Mandelkow, 1993), using cryo-ET and subtomogram averaging of MTDs decorated with monomeric kinesin rk354 (Figures 2A and 2B; Figure S1A and S1B), we successfully distinguished β-tubulin from α-tubulin for all the PFs in the B tubule (PF-B1–B10) and five of the A tubules (PF-A2, A4, A5, A8, A9), as seen in Figure 2B (for PF-A5 and PF-B1) and Figure S2 (for all the other PFs). Based on this assignment, we concluded that the lattice arrangement of the B tubule is B lattice. We could not conclude the same for the A tubule, as it was not possible to decorate all PFs of the A tubule with kinesins due to presence of outer proteins such as dyneins and RSs. ODA binds to PF-A6 and A7, IDA binds to PF-A4, and RS binds to PF-A2 and A3. PF-A1 and A10–A13 are part of the ribbon region and hence are inaccessible to bind kinesin. Kinesin still partially binds to PFs A2 and A4, enabling us to identify isoforms (Figure S2). As B-tubule staggers are observed between PF-A4 and A5, and between PF-A8 and A9 with identified tubulin subunits in the A tubule, the lattice arrangement of the A tubule is also likely to be B lattice as proposed by Song and Mandelkow (1993) (Figure 2D). However, as kinesin binding was not found on PF-A1, A3, A6, A7, and A10–A13, there is still a possibility that few of these PFs take A-lattice staggers.

Another interesting finding is the density connection between subunits mentioned in the previous section. In PF-A2, A4, and A5, and PF-B1–B6 and B8–B10, where tubulin isoforms have been assigned decisively based on kinesin binding, we found a density connection between two adjacent subunits. In all these PFs, the interface between subunits inside a dimer (intra-dimer interface) has higher density than between dimers (inter-dimer interface), as shown in Figure 2B (PF-A5 and PF-B1; kinesin heads are indicated by arrows) and Figure S2 (PF-A2–A4 and PF-B2–B6, B8–B10). This suggests that arrangement of the dimers can be determined by the differential densities between tubulin subunits at the inter-dimer and intra-dimer interface, as is also seen in the reconstituted microtubule (Figure 2C).

Assignment of α- and β-Tubulin Subunits by Image Analysis

For the PFs A1, A3, A6, A7, and A10–A13 where the tubulin isoforms could not be identified by kinesin binding, we tried to assign the tubulin isoforms based on image analysis. As distinguishing criteria, we used (1) continuity of density within a dimer, which we found in PFs A3, A4, A5, A8, A9, and B1–B10 and (2) CCC between our 19-Å density map and the pseudo-atomic model of the PF. In all the PFs that have both kinesin binding and density continuity within a dimer (PF-A1–A6; PF-B1–B6, B8–B10), assignments based on kinesin binding and continuity are consistent with each other. Therefore, we also attempted to assign the pattern of tubulin isoforms based on CCC. We generated the pseudo-atomic model of the PF (96 nm length) which has a best fit to the high-resolution MTD structure from single particle analysis (for details see Experimental Procedures). We calculated the CCC between our density map of MTD and the density map of the PF calculated from the pseudo-atomic model. We also calculated the CCC using the pseudo-atomic model shifted by 4 nm. Comparing these CCC values (Table 1), we could judge which position of the pseudo-atomic model is more likely fitted to the EM density map. Although the difference between the CCC values is not very apparent in some PFs, it supported our assignment of tubulin isoforms based on either kinesin decoration or density continuity within a dimer, except B10, in which CCC is lower with our assignment based on kinesin and density continuity (we speculate that this is due to large density of MIP beside B10). We found that the isoform assignment is consistent with kinesin-based assignment for PFs A2, A4, A5, and B1–B10. It also corroborates with our observation that density is more continuous in the intra-dimer interface than in the inter-dimer interface in PFs A2–A6, A11–A12, B1–B6, and B8–B10 (Figure S2): according to the isoform assignment based on CCC, continuous density is found within a dimer. Therefore it is reasonable to characterize the pattern of tubulin isoforms in all the PFs except B10 based on CCC values and the density at intra- and inter-dimer interface (Figure 2; Figure S2). PF-A10 did not show clear difference of CCC between our EM density and the atomic model with 4-nm shift, and moreover we could not find a difference in connection between adjacent subunits, leaving the assignment of isoforms for PF-A10 still ambiguous (the assignment of A10 based on CCC is shown in Figure S2). Even with this ambiguity located between A9 and A11, we can conclude that the arrangement of A tubule is B lattice (Figure 2D).

The assignment of the tubulin subunits indicates the presence of a seam between PF-A9 and A10 or between PF-A10 and A11 (according to CCC-based assignment, it is between PF-A10 and A11). This means that the seam is closer to the outer junction (Figure 2C). As tubulin subunits for all PFs (except A10) were assigned, we calculated the axial staggers between protofilaments in the A and B tubules. The stagger of tubulin subunits between adjacent PFs in the ribbon region (0.58 ± 0.05 nm) is significantly smaller than what is expected in a B lattice (0.92 nm), compared with the rest of the A tubule (0.97 ± 0.14 nm) and the complete B tubule (0.90 ± 0.12 nm) (Figure 2E).

Microtubule Inner Proteins

The class of proteins known as MIPs has been previously reported in *T. thermophila*, *C. reinhardtii*, and sea urchin sperm (Linck et al., 2014; Nicastro et al., 2011; Pigino et al., 2012; Sui and Downing, 2006). MIPs 1–4 were commonly observed among these species. Taking research in this area a step further, our high-resolution structural analysis with *T. thermophila* shows the presence of additional MIPs, and the structures of known MIPs were revealed in more detail (Figure 3B), while no MIP found by tomography (Pigino et al., 2012) was lost in this single particle analysis study. Docking the 23-Å MTD structure to the pseudo-atomic model of tubulin (described in the previous section) enabled us to identify the periodicity and detailed positions of the MIPs binding in the lumen of both A and B tubules. In our study, MIPs 1–4 were shown to have different structures from those given in the previous reports (Nicastro et al., 2011; Pigino et al., 2012), probably due to the resolution limitation of cryo-ET and species differences. In *Chlamydomonas*, MIP1 makes an arch-like structure, connecting PF-A5 and A6 (Figure 3C of Pigino et al., 2012; Figures 4B and 4D of Nicastro et al., 2011), whereas in *Tetrahymena* it is much smaller and only binds to PF-A5 (Figure 3B). In *Chlamydomonas*, MIP2a and MIP2b have distinct morphologies and sizes (Linck et al., 2014; Nicastro et al., 2011), whereas at current resolution, in *Tetrahymena* the slight differences between MIPs 2a and 2b become more evident (Figure 3B). MIP3a and MIP3b make a cage-like structure surrounding PFs A1, A13, B10, and B9, keeping the A and B tubules together at the inner junction of the MTD (Figures 3B and 3C). The position of MIP3 matches that of FAP20 in *C. flagella* (Yanagisawa et al., 2014), suggesting that FAP20 is at least one component of MIP3. At the outer junction, a continuous laminar sheet connecting PF-A11 to PF-B1 is found (Figures 3B and 3C). At lower resolution, MIP4 barely appeared, and the position and periodicity could not be well characterized (Nicastro et al., 2011; Pigino et al., 2012). At our current resolution we could distinctly identify three components (MIP4a, 4b, and 4c) appearing on

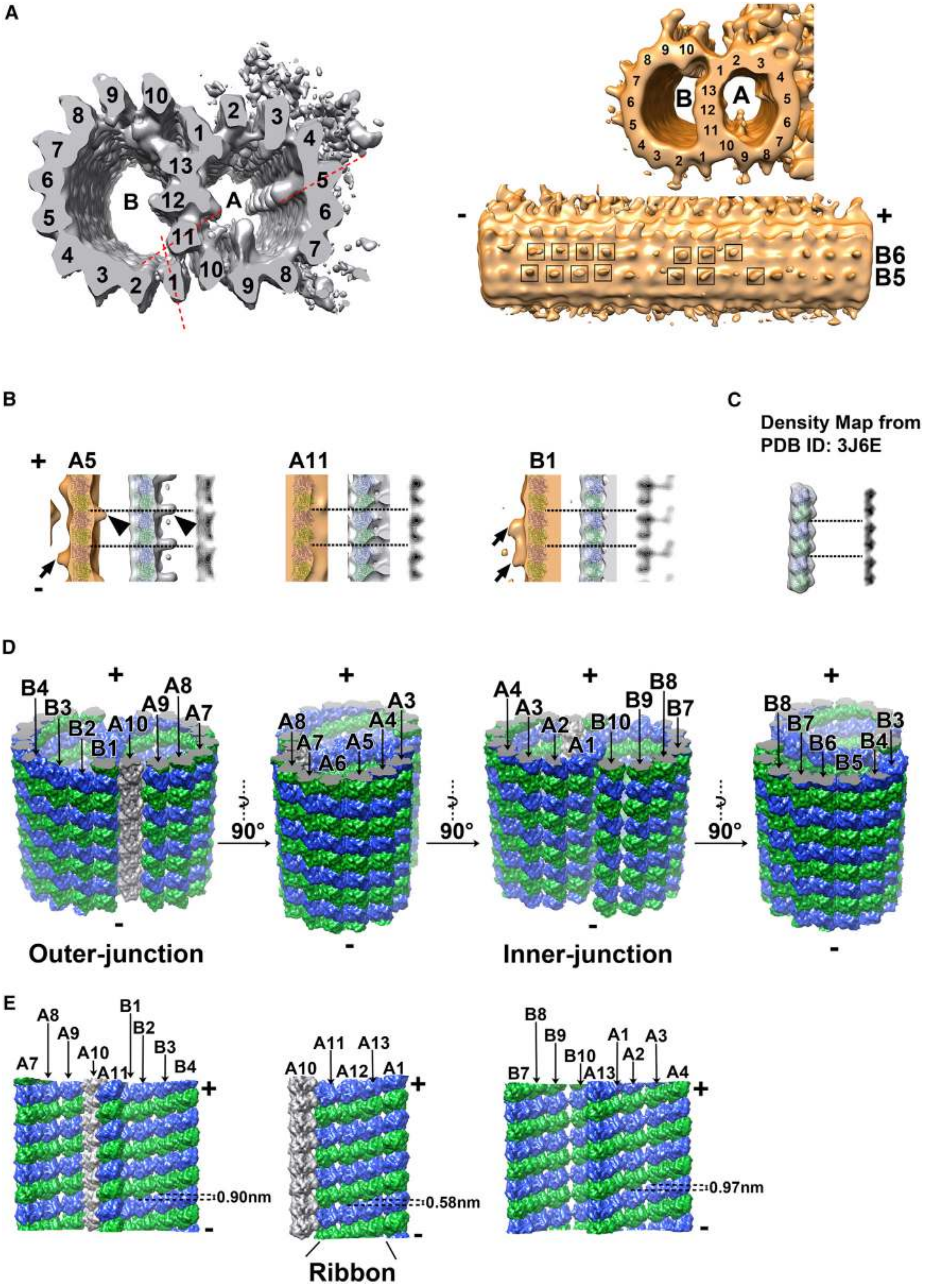

Figure 2. Assignment of Tubulin Subunits Using Single Particle Analysis and Electron Tomography

(A) (Left) Single particle analysis of MTD (the protofilaments have been numbered based on Linck and Stephens, 2007). (Right) Subtomogram average obtained using cryo-electron tomography of kinesin-decorated MTD. Top: View from the tip of cilia (plus end of MT). Bottom: Side view; kinesin-heads binding to PF-B5 and B6 are indicated by black rectangles, showing the B-lattice stagger.

(B) Longitudinal sections (parallel to the planes indicated by the red dashed lines in A). Left of each panel: cryo-ET of kinesin-decorated MTD (ocher) with fitted atomic models of tubulin isoforms identified based on kinesin binding (green: α; blue: β). Center of each panel: single particle analysis of MTD. Density

(legend continued on next page)

Table 1. Assignment of PFs

Protofilament Number (* Indicates Kinesin Decoration)	CCC Value (as Fitted)	CCC Value (Shifted 4 nm)	Continuity within the Dimer
A1	0.7879	0.7871	yes
A2*	0.7903	0.7681	yes
A3*	0.9031	0.8996	yes
A4*	0.9099	0.9058	yes
A5*	0.9282	0.9186	yes
A6	0.9475	0.9389	yes
A7	0.9290	0.9252	no
A8*	0.9086	0.8941	no
A9*	0.8800	0.8678	no
A10	0.8653	0.8637	no
A11	0.9393	0.9362	yes
A12	0.9401	0.9369	yes
A13	0.9174	0.9166	yes
B1*	0.7939	0.7847	yes
B2*	0.8960	0.8900	yes
B3*	0.9502	0.9437	yes
B4*	0.9567	0.9544	yes
B5*	0.9581	0.9555	yes
B6*	0.9550	0.9462	yes
B7*	0.9237	0.9191	no
B8*	0.8499	0.8440	yes
B9*	0.8736	0.8716	yes
B10*	0.9002	0.9033	yes

PF-A10, A11, and A12 (Figures 3B and 3C). The apparent periodicity is 16 nm, whereby the distances between MIPs 4b and 4c and between 4c and 4a are each 4 nm. MIP5 and MIP6 were identified for the first time and were named sequentially. MIP5 binds every 16 nm along PF-A12, facing toward the lumen of the B tubule (Figures 3B and 3C). MIP6 is a complex, continuous structure spanning PF-A1, A2, and A3 every 8 nm (Figures 3B and 3C). The periodicity of MIPs 1–3 is conserved between *Tetrahymena* and *Chlamydomonas*.

Binding of MIPs

MIPs were distinctly located either on or between the PFs, either on a tubulin subunit or bridging the two subunits of a dimer. The elements of MIP4 bind between PFs, while MIPs 2, 3, and 6 span across two or more PFs (Figure 3C). MIPs 1 and 5 are on individual PFs (Figure 3C). Except for MIPs 3 and 5, all the MIPs bind in the lumen of the A tubule (Figure 3A).

MIPs 1a (molecular weight [MW] $\sim$18 kDa; based on the calculation of the volume in chimera, such that the density is enough to cover the MT) and 1b (MW $\sim$4 kDa) bind between two tubulin dimers on PF-A5 (Figure 3B). MIP2a and MIP2b (both with MW $\sim$41 kDa) bind β-tubulin and alternate every 16 nm along PF-A9, connecting to MIP4c without contacting PF-A10 (Figure 3C). MIP3a (MW $\sim$90 kDa) has a unique structure, connecting the A and B tubules to each other in an interesting manner (Figure 3C). MIP3a binds on PF-B10 with a wide interface and also connects to PF-B9 via α-tubulin. Another branch of MIP3a binds to α- and β-tubulin on PF-A13. MIP3b binds to α-tubulin on PF-A13, and to β-tubulins on PF-B10 and B9. Both MIP3a and MIP3b (MW $\sim$15 kDa) contact PF-A1 as well. MIP4a (MW $\sim$12 kDa) and MIP4b (MW $\sim$6 kDa) bind to α-tubulins on PF-A11 and A12, whereas MIP4c (MW $\sim$3 kDa) binds to β-tubulins on PF-A11 and A10 (Figure 3C). MIP5 binds between the tubulin subunits of a dimer on PF-A12 (Figure 3C). MIP6 (MW $\sim$11 kDa) has the longest span within the A tubule, binding to α-tubulins on PF-A1 and A3 as well as between the tubulin subunits of a dimer on PF-A2 (Figure 3C).

Binding of Dyneins and Radial Spokes

To identify the locations of various outer binding proteins such as dyneins and RSs, the medium-resolution tomographic structure of MTD (EMD: 2132) (Bui et al., 2012) (Figures 1G and 1H) was fitted with the pseudo-atomic model derived from our high-resolution MTD structure from single particle analysis (Video S1). All the IDAs bind on PF-A3 and A4 (Figure 4A). In this study, we call inner arm dynein isoforms based on their loci following the naming in *Chlamydomonas* flagella (Bui et al., 2012). It is known that the tails of dyneins a, c, g, and d are fused with the base of RSs, and dynein e is fused with the DRC (Bui et al., 2008; Pigino et al., 2012). In our analysis, dyneins a, b, c, e, and g bind to the tubulin backbone, all emerging from β-tubulins of PF-A3 and settling on PF-A4 (Figure 4A). The interface covers most of the external surface of the β-tubulin of PF-A3 and $\sim$4-nm proximal site on PF-A4 (blue atomic models in Figure 4A). However, there is slight variation of interfaces for inner dynein species. Dyneins a and e fully settle on β-tubulins of PF-A3, while dyneins b, c, and g stem from the boundary between two adjacent dimers of PF-A3.

The three RSs bind on PF-A2 and A3 (Figure 4B). RS1 and RS2 bind to the dimers of PF-A2 and A3. In our previous

---

corresponding to one PF is presented as a gray surface-rendered model with fitted atomic models. Right of each panel: contour and gradient density maps from single particle analysis (black: high density; white: low density; contour lines are shown in white). The contour and gradient density maps were calculated from the projection of slabs of 30 Å thickness, enough to cover a tubulin molecule. Only the high-density core part is shown to highlight the difference in density continuity at the intra- and inter-dimer interface. Dimers were assigned based on either kinesin binding or density continuity in the contour map. Only PF-A5, A11, and B1 are shown. The other PFs are shown in Figure S2. The arrows and arrowheads indicate kinesin heads and MIPs, respectively. Luminal side of all PFs is on the right. Proximal (−) and distal (+) ends are indicated in PF-A5 and apply to PF-A11 as well as B1.

(C) Sections from a reconstituted microtubule (low-pass filtered from 3J6E). In (B) and (C), each dimer is indicated by horizontal dotted lines.

(D) Oblique perspective views of the MTD model as seen from the outside, showing the lattice arrangement of A and B tubule as well as outer and inner junctions. The model was generated by low-pass filtering (to 12 Å) the fitted pseudo-atomic model and trimming. Objects farther away from the reader are shown in pale colors. PF-A10 is colored gray, as we could not decisively identify the pattern of the isoforms.

(E) View of the outer junction (left), ribbon (center), and inner junction (right) as seen from the inside of the MTD. The average axial stagger of tubulin subunits between adjacent PFs within the B tubule, ribbon, and A tubule is indicated in the left, center, and right panel, respectively. Proximal and distal ends are indicated with – and +, respectively.

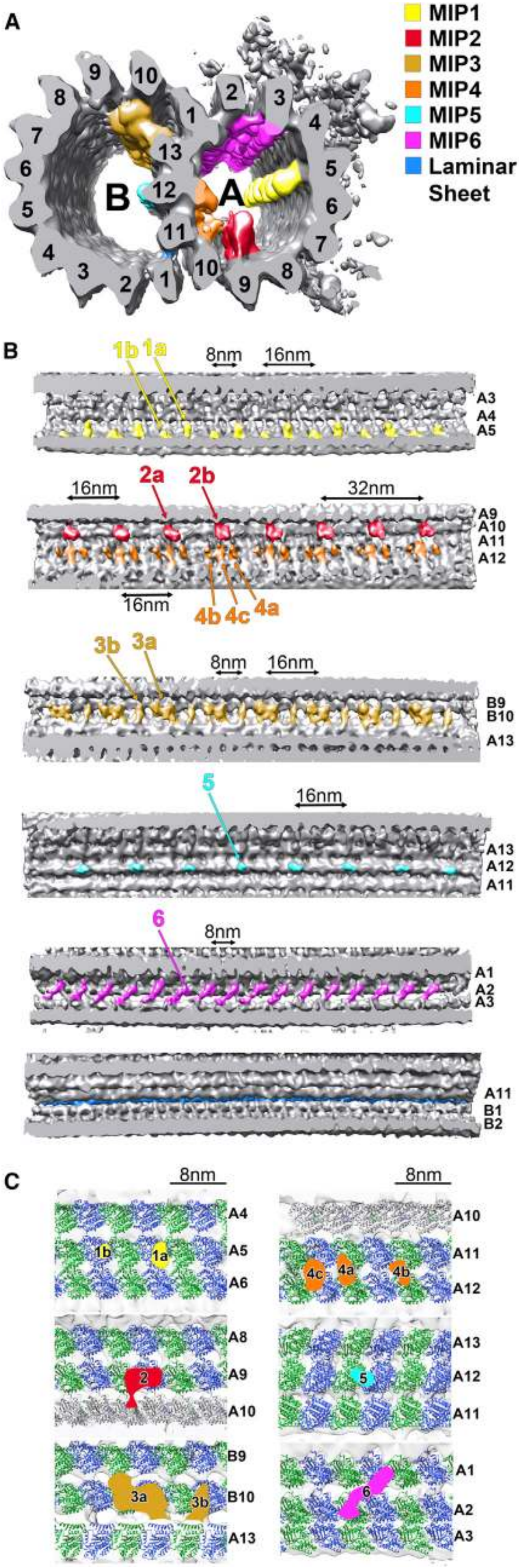

Figure 3. Location and Conformation of MIPs in the Single Particle Analysis Map

(A) Surface-rendered cross section of the MTD seen from the tip of cilia, depicting the location of various MIPs (MIPs 1–6 and laminar sheet), their binding to the PFs, and the distortion of A tubule. The numbers of protofilaments in A- and B-tubules are indicated.

(B) Longitudinal sections (sectioned parallel to the MTD axis) of MTDs showing the periodicity and location of various MIPs and the laminar sheet. Each MIP has its characteristic density and pattern along the PF. The distal end is at the right. Distances between MIPs are indicated. PFs are labeled at the right and seen from the inside of MTD.

(C) MIPs juxtaposed on the pseudo-atomic model of MTD. Green, α-tubulin; blue, β-tubulin. To compare the positions of MIPs easily, the frames of the panels are fitted to have α- and β-tubulins approximately at the same position.

tomography study (Pigino et al., 2011), the distance between RS1 and RS2 was 32 nm, four times the 8-nm tubulin periodicity. However, in Figure 4B the interfaces to the microtubule are significantly different between RS1 and RS2, probably due to the difference of adaptor proteins. RS3 is known to be different from RS1 and RS2, both structurally and in terms of components (Pigino et al., 2011). Indeed, our structural study proved that the binding site of RS3 is different from RS1/RS2: it appears mostly to bind to one dimer of PF-A3, while RS1 and RS2 bind both PF-A2 and A3 (Figure 4B). Details of binding types and sites for various outer and inner proteins are summarized in Table 2.

Microtubule-Binding Domain of Outer Arm Dyneins

We examined the location of the MTBD at the tip of the outer arm dynein stalk on MTD. Normally MTBD did not appear in the average of MTD using 96- or 24-nm periodicity. This was because we detected periodicity based on dyneins binding to the A tubule via tails and not based on dyneins binding via MTBD to the B tubule, at the opposite side of the MTD. Therefore, MTBDs were averaged out. In this study, we classified averages of subtomograms extracted from individual MTDs from *Chlamydomonas ida1* mutant in the absence of additional nucleotides (Bui et al., 2012) to see MTBDs, and obtained three classes (Figure 5A). These show identical structures of MTD and dynein binding to the A tubule, but the positions of MTBDs, and therefore ODAs on the adjacent MTD, vary. The position of ODAs on the adjacent MTD in classes 2 and 3 are shifted 8 and 16 nm along the MTD relative to class 1. Also, in each class, the γ-dynein on the MTD is axially located at the same position as the β-dynein on the same MTD (Figure 5A). The axial shift of the ODAs between the three classes indicates a relative shift (8 or 16 nm) between adjacent MTDs. The position of MTBD on MTD in all three classes is consistent with our atomic model fitting and is between α- and β-tubulins within a dimer (Figure 5B). This means that MTBD binding to the B tubule is at the same position as the cytoplasmic dynein dimer (Redwine et al., 2012) and independent of the binding of dyneins on the A tubule.

DISCUSSION

Lattice of α/β Tubulins

Our single particle analysis of MTD, cryo-ET of MTD decorated by kinesin heads, and 3D image analysis showed that both A

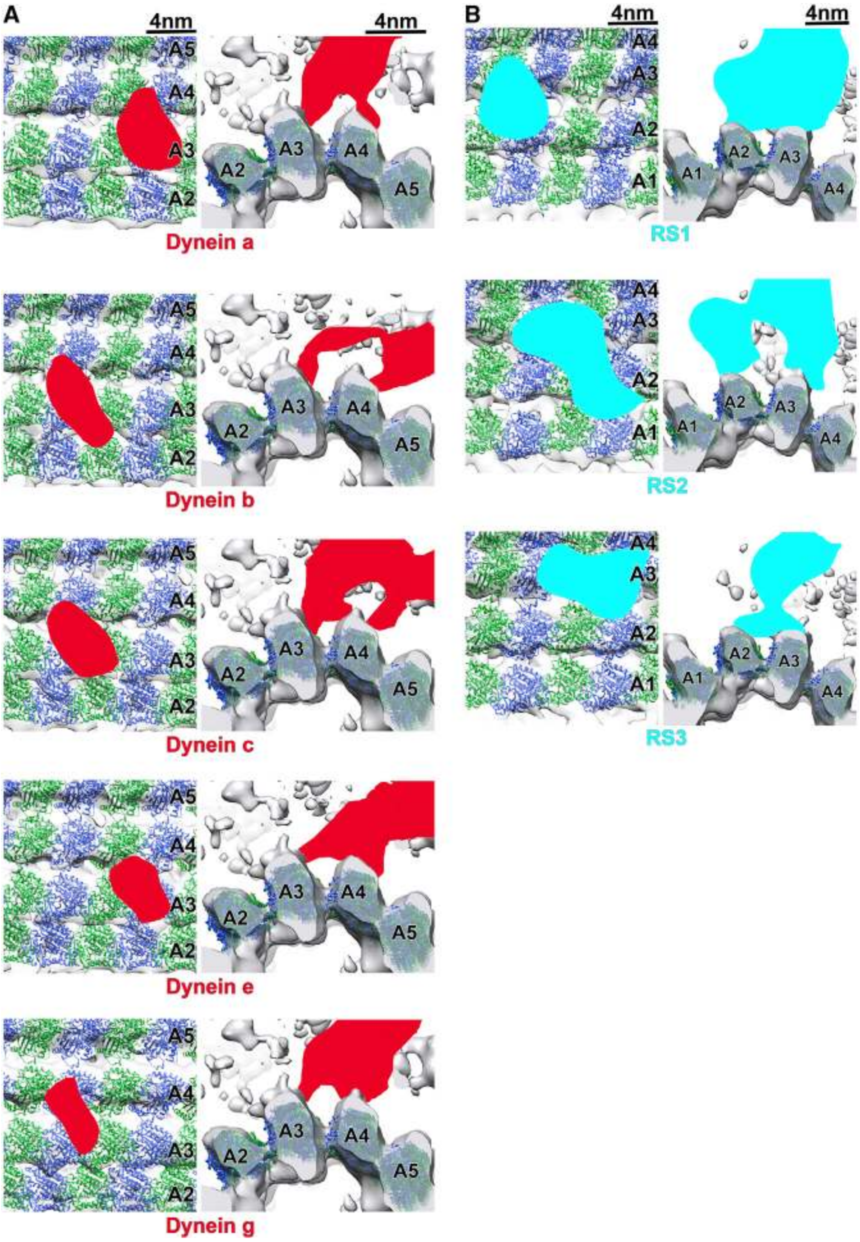

Figure 4. Details on Binding of Inner Arm Dyneins and Radial Spokes

Surface-rendered longitudinal and cross sections of the MTD (from single particle analysis), depicting the binding of various IDAs and RSs to the PFs. IDAs from tomography (EMD: 2132) are juxtaposed in red in (A) and RSs in cyan in (B). IDAs (dyneins a, b, c, e, g) bind in a similar style to the backbone of PF-A3 and A4. RSs appear to bind similarly, spanning over PF-A2 and A3. In the longitudinal sections the proximal end is at the left and distal at the right. In the end-on views, the distal end is oriented toward the reader. Green: α-tubulin; blue: β-tubulin.

and B tubules of MTD have the B-lattice arrangement. The seam of the A tubule is placed close to the outer junction, either between PF-A9 and A10 or PF-A10 and A11 (Figures 2D and 2E; Video S1). This observation is in contrast to the proposed presence of the seam close to the inner junction, which was based on a negative-stain EM study with kinesin decorated on the tubulin sheets extending from open MTD sheets (induced by adding exogenous brain tubulin to the MTD) (Song and Mandelkow, 1995). Although there might be reservation in our tubulin assignments for PF-A10 to A13 (ribbon region), which lacks direct evidence from kinesin binding, the tubulin assignments at the outer junction based on kinesin binding also show discrepancy between our current work and their work: at the outer junction PF-A9 and PF-B1 are shifted 4 nm (Figure 2D), while in their work corresponding PFs are in the same order. At the inner junction, PF-B10 (Figure 7 of Song and Mandelkow, 1995) and PF-A2 are in the same order, showing agreement between our results and theirs. The procedure used by Song and Mandelkow (1995) may have caused rearrangement of PFs during the extension. Judging from the fact that the reconstituted MTs have a B-lattice arrangement, adjacent PFs are likely more stable in the B-lattice type configuration and they adopt the A-lattice configuration only when the cylindrical geometry does not allow a continuous B lattice, hence a seam results.

MIPs

All the MIPs found in this study have periodicity of integer times of 8 nm, indicating connection to tubulin periodicity. MIPs 3a and 3b are localized between PF-A1, A13 and PF-B9, B10. This is the same position as that of FAP20 proved by biotin-carboxy carrier protein tagging (Yanagisawa et al., 2014). Since the MW of FAP20 is 22 kDa, MIP3a (volume corresponding to 90 kDa) is likely a candidate of a complex involving FAP20, although the possibility of FAP20 flexibly existing at the MIP3b position cannot be excluded. While the past report assigned the density on the ribbon and inside the A tubule to a filamentous structure (Linck et al., 2014), our analysis indicated that MIP4 has rather discontinuous density (Figures 3B and 3C), and filamentous density exists on the ribbon but outside the A tubule (Figure 3A).

The structure of MIPs raises a number of questions and suggests speculations regarding these uncharacterized proteins inside MTDs. Why do so many types and subtypes of MIPs exist? What do the differences in the structure and distribution of these molecules reflect in terms of their function? Although MIP structure appears different in various species, the periodicity is conserved, suggesting a common function in all motile species. During bending shear forces should arise between adjacent MTDs, and flagella need to be robust enough not to fall apart, yet at the same time be flexible enough to allow sliding and

Table 2. Binding Location of Outer and Inner Proteins

Proteins	Binding Locations
MIP 1a, 1b	A5[‡,○]
MIP 2a, 2b	βA9[‡,○], A9/A10[‡,●]
MIP 3a	B9/A13[†,●]
MIP 3b	βB10/αA1[+,●]
MIP 4a	αA11/A12[+,●]
MIP 4b	αA11/A12[+,●]
MIP 4c	βA11[+,○]
MIP 5	A12[‡,○]
MIP 6	αA1[+,●], A2/A3[†,●]
Dynein a	A3/A4[†,●]
Dynein b	A3/A4[‡,●]
Dynein c	A3/A4[‡,●]
Dynein e	βA3/αA4[+,●]
Dynein g	A3/A4[‡,●]
RS 1	A2/A3[†,●]
RS 2	A2/A3[†,●]
RS 3	βA2/A3[+,●]

Dynein d position could not be precisely located.

[+] Binding on one subunit of the dimer.

[†] Binding between subunits of the dimer.

[‡] Binding between dimers.

[○] Binding on a protofilament.

[●] Binding between protofilaments.

bending. The PFs composing each MTD should experience a similar stress. We observed that most of the MIPs bind not only to a single PF but interact with two or three PFs (Figure 3; Table 2). The lattice distortion in the A tubule was ~20% (Figure 2A), meaning that PFs do not follow an exact helical arrangement distinguishing it from a 13-PF MT. Further observations revealed that at some places where MIPs are found, the distance between adjacent PFs appears to be abnormally wide (PF-A1–A2, A9–A10, and A4–A5 in Figure 3A). These facts suggest that the MIPs are a key factor in distinguishing the MTD from the cytoplasmic MT both structurally and functionally. Such a distortion in the tubule does not compensate for the presence of the seam, which is a common feature of the doublet and the singlet. It is not yet clear whether the presence of MIPs causes the distortion or whether the MIPs help maintain the integrity of the distorted PFs.

The diverse binding sites for the inner and outer MTD-binding proteins might reflect the diverse functions they perform. So far, we know that the dynein stalk binds on a single PF between the two subunits of a dimer (Redwine et al., 2012), and although kinesin and dynein share an overlapping MT-binding site (Mizuno et al., 2007), they move in opposite directions and carry different cargoes. On the other hand, EB1 binds between PFs (Maurer et al., 2012). Our study revealed that a few inner and outer proteins bind on PF (e.g. MIP5), others bind between PFs (e.g. MIP6), and a few have multiple binding sites (e.g. RSs, dynein tails, and MIP3). Similarities in binding site might suggest common binding mechanisms or conserved binding domains, although it is difficult to comment further on the similarity in mechanism or function at the current resolution.

EXPERIMENTAL PROCEDURES

MTD Preparation

The *T. thermophila* SB210 strain used in this study was obtained from the Tetrahymena Stock Center (Cornell University) and cultured in protease peptone medium (Orias et al., 2000). Cilia were isolated using the dibucaine method to induce deflagellation (Witman, 1986). In detail, cells were exposed to 2 mM dibucaine and the reaction was stopped after 2 min with 30 mM HEPES (pH 7.4), 5 mM $MgSO_4$, 1 mM DTT, 0.5 mM EDTA, 25 mM KCl (HMDEK buffer), and 4 mM $CaCl_2$. Extracted cilia were sedimented at 9,500 × *g* for 15 min at 4°C, demembraned with HMDEK buffer and 0.8% NP-40, and sedimented again. MTDs (split axonemes) were obtained by exposing the demembraned cilia to 0.4 mM ATP (Maheshwari and Ishikawa, 2012) and further washing with 0.6 M NaCl to remove the dyneins (Figure S1C). Taxol was not added throughout this preparation. Washed MTDs were sedimented at 9,500 × *g* for 15 min at 4°C. Protein concentration was determined according to the Bradford method (Bradford, 1976) using BSA as the standard.

Protein Expression and Purification

Monomeric kinesin, rk354 (aa 1–354 of Kif5c), was constructed by PCR from the rat kinesin *Kif5c* and cloned into a modified pET-32a vector (Novagen) with a C-terminal His_6. After Gly234Ala mutation, the construct was expressed in *Escherichia coli* BL21-CodonPlus (DE3) RIL (Stratagene). This mutant binds to microtubules with high affinity but is deficient in ATP hydrolysis and does not move on microtubules (Rice et al., 1999). Cells were collected, resuspended in buffer A (20 mM PIPES-KOH [pH 6.8], 300 mM KCl, 0.1 mM ATP, 1 mM $MgSO_4$, 0.01 mM EGTA, 0.5 mM DTT, and 10 mM imidazole), supplemented with Complete Mini, EDTA-free (Roche), and lysed. Following centrifugation, the soluble protein in the supernatant was purified by Ni-IMAC resin (Bio-Rad) and eluted with buffer B (20 mM PIPES-KOH [pH 6.8], 300 mM KCl, 0.1 mM ATP, 1 mM $MgSO_4$, 0.01 mM EGTA, 0.5 mM DTT, and 300 mM imidazole). The elution buffer was exchanged with BRB80 (80 mM PIPES-KOH [pH 6.8], 1 mM EGTA, and 1 mM $MgCl_2$) with a NAP-5 column (GE Healthcare). The purified rk354 (G234A) was aliquoted at a concentration higher than 1 mg/ml and frozen under liquid nitrogen.

Kinesin-Decorated MTD

The kinesin-binding preparation was done directly on the plasma-cleaned EM grid, just before freezing. After depositing 3 μl (0.5 mg/ml) of the washed MTDs on the grid, 3 μl of assay buffer (50 mM imidazole, 5 mM Mg-acetate, 1 mM EGTA, 50 mM K-acetate, 10 mM DTT, 0.1% Triton X-100, 2 mM 5-adenylyl imidodiphosphate) was added, followed by addition of an equimolar concentration of kinesin (rk354).

Data Collection for Cryo-ET and Single Particle Analysis

For single particle analysis of MTD, 3 μl (0.5 mg/ml) of washed and separated MTDs was deposited on the grid. The grids with frozen-hydrated samples were transferred to a Tecnai F20 transmission electron microscope (FEI) at 200 kV by a Gatan 626 cryoholder (Gatan) cooled by liquid nitrogen. Micrographs were collected with the 4k × 4k Gatan UltraScan 4000 CCD camera, at 67,000× nominal magnification, and with the defocus ranging from 2 to 4 μm. The electron dose on the sample was between 15 and 25 e/Å^2.

For the cryo-ET of kinesin-decorated MTD, after the addition of monomeric kinesin, 3 μl of 10-nm gold colloidal particles were applied to the grids, and the grids were then plunge-frozen. Images were collected as described previously (Bui et al., 2008, 2009; Movassagh et al., 2010; Pigino et al., 2011) using an energy filter (Gatan GIF Tridiem), and a 2k × 2k CCD camera (Gatan UltraScan 1000). Exposures were made at a nominal magnification of 19,303× and an underfocus of 3–5 μm. Tomographic image series from −60° to 60°, with 2° tilt increments, were acquired using Explore3D software (FEI). Images were collected with an exposure time of 0.1–0.2 s and energy filter width of 20 eV. The total dose was between 30 and 60 e/Å^2.

Single Particle Analysis of 96-nm Repeating Unit of the MTD

For single particle analysis, micrographs with high defocus and astigmatism were rejected and the rest were used for particle picking (using x3d [Conway and Steven, 1999]) based on the 96-nm periodicity of RS. We used particles

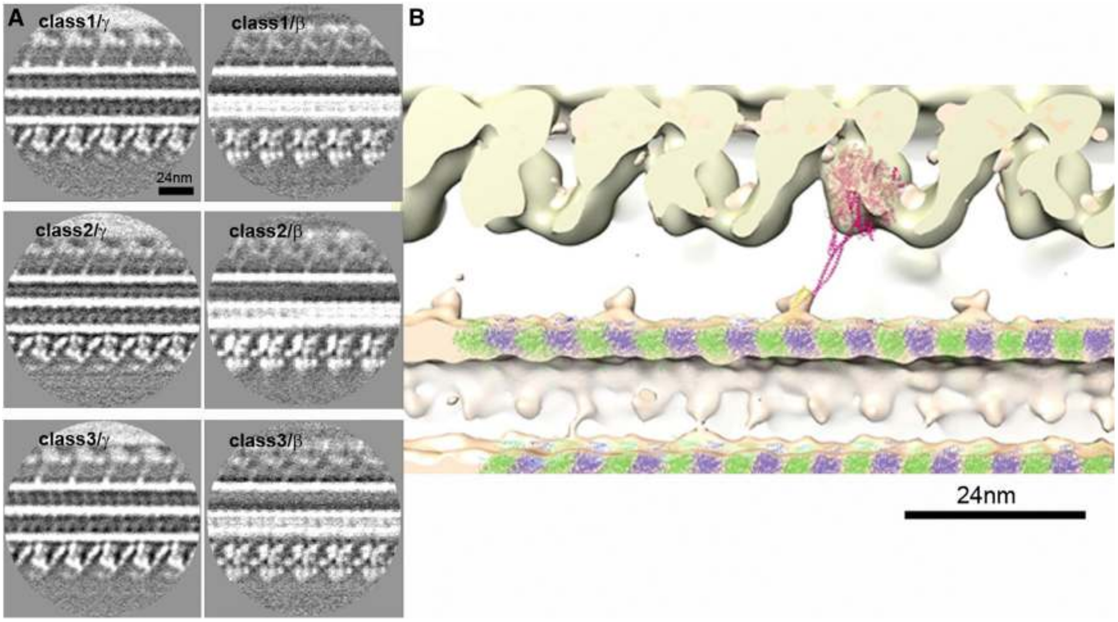

Figure 5. Binding of MTBD of Outer Arm Dyneins on MTD as Shown in Classified Subtomogram Averages

(A) Sections of MTD from *ida1* mutant of *Chlamydomonas* after classification of subtomograms based on the positions of MTBD of outer arm γ dyneins extended from the adjacent MTD. Sections of γ and β dyneins are shown in the left and right panels, respectively.

(B) Surface rendering with atomic models of cytoplasmic dynein (PDB: 3VKG) (Kon et al., 2012) (shown in purple) and tubulins (green, α-tubulin; blue, β-tubulin) fitted to MTD from our single particle analysis (pink). Atomic models of dyneins were fitted to the density of the γ-dynein. MTBD binds between α- and β-tubulins within one dimer.

from all MTDs, since there is no asymmetrical molecular arrangement found in *Tetrahymena* cilia (Pigino et al., 2012), unlike in *Chlamydomonas* (Bui et al., 2012). CTF parameters were measured from each micrograph, and phase flipping was applied to each particle. Projection matching was performed using the tomographic structure of *Tetrahymena* MTD in the intact axoneme (Pigino et al., 2012) as the initial reference. Initially, each particle was low-pass filtered at 20 Å and high-pass filtered at 500 Å (Butterworth filter), matched with projections from the reference, and aligned accordingly. Projection matching was limited within 30° of elevation angles with respect to the horizontal plane, since MTDs mostly show side views (Figure S1D). Particles matching the same projection were classified and averaged together. All the class averages were further back-projected to achieve the final 3D structure. The procedure was repeated for 40 iterations. After ten iterations, the projections were made from the updated reference at smaller angular difference. For the final round of iteration, projections were made at every 2°. Ultimately 10,700 segments were used. The resolution of the final structure was 23 Å using the criterion of 0.143 as the gold standard refinement FSC (Rosenthal and Henderson, 2003) of two reconstructions from two groups (each containing 5,350 segments) aligned in the final iteration. All steps from CTF correction to 3D structure calculations were performed with SPIDER (Frank et al., 1996).

Reconstruction of 16-nm Repeating Unit of the MTD

Since most of the MIPs in the 96-nm repeating unit of the MTD have periodicity of 16 nm, we attempted to obtain the structure of the 16-nm repeating unit of the MTD from the 96-nm unit map as this would be equivalent to a 6-fold increase in input data. Six 16-nm repeating units were boxed out from the 96-nm single particle analysis map, aligned, and averaged together, giving rise to a 3D structure at an improved resolution of 19 Å.

Surface rendering and visualization of all maps was done using UCSF Chimera software (Pettersen et al., 2004). Contour maps were generated by MATLAB image processing toolbox (MathWorks).

Subtomogram Averaging of Kinesin-Decorated MTD

Tomograms of kinesin-decorated MTD were reconstructed by IMOD (Kremer et al., 1996) with fiducial marker alignment and R-weighted back-projection. The averaged tomographic map of the 96-nm repeating unit of the kinesin-decorated MTD showing RS or dynein was obtained as described in detail by Bui et al. (2008, 2012). The structure of *Tetrahymena* MTD in the intact axoneme (Pigino et al., 2012) (MTD without kinesin) was used as the initial reference for the kinesin-bound MTD.

Datasets with no RS or dynein could not be included in the initial average. These subtomograms along the same MTD were aligned and averaged. The polarity of the MTD was determined based on the polarity of kinesin, with the kinesin head facing downward toward the plus end of the MTD (Figure S1A). After that, those subtomograms were aligned with the averaged map with RS and dynein and combined into a final average. This alignment may cause a 48-nm shift, which does not affect the assignment of tubulin isoforms. Localization of kinesins bound to the MTD was done by comparing the final kinesin-bound MTD tomographic map with the unbound MTD (Pigino et al., 2012) (Figures S1A and S1B).

Building the Pseudo-Atomic Model of the MTD and the Assignment of the Tubulin

The pseudo-atomic model of MTD based on our single particle analysis from *T. thermophila* was built by fitting the atomic model (Alushin et al., 2014). We initially fitted their atomic model of PFs to our structure and adjusted the position of tubulin dimers to maximize CCC, assuming that the tubulin dimer is rigid. We made another pseudo-atomic model by shifting the atomic models 4 nm along MTD and fitting them to our map. CCC was calculated by low-pass filtering the atomic models to 20 Å, with the threshold of the doublet structure such that the atomic models were sufficiently overlapped with the structure (1%–4% atoms outside the contour). Only the data above the contour level from the first map were used. The CCC values for both of the PF models are listed in Table 1. Similar CCC analysis with exact conditions was also performed with the pseudo-atomic model, low-pass filtered at 15 and 25 Å, and the assignment turned out to be the same, which strengthened our computational assignment.

To distinguish between the α- and β-tubulin in a PF, another approach using kinesin decoration was taken: for PFs-A2–A5, A8, and A9 as well as all the PF-Bs, the kinesin-decorated MTD structure obtained from cryo-ET was docked to the structure obtained from single particle based on CCC. This docking shows obvious matching of MIPs (Figure 2B; Figure S2). The α- and β-tubulin assignment based on the CCC analysis of all the PFs that bind kinesin was consistent with the assignment based on kinesin binding, proving that tubulin isoforms were correctly identified for all the PFs that bind kinesin heads.

Locating the Binding Sites of MTD Proteins

To locate the binding sites of various MIPs, the structure obtained from single particle analysis fitted with the correctly assigned pseudo-atomic model was used. To locate the binding sites of dyneins and RSs, the above docked structure and pseudo-atomic model was further fitted to the structure of the 96-nm repeating unit of MTD obtained from cryo-ET with subtomogram averaging of *Tetrahymena* axoneme (Pigino et al., 2012), using the "Fit In Map" function of UCSF Chimera.

Analysis of the *Chlamydomonas ida1* Mutant

To visualize ODAs from the adjacent MTD, we classified subtomograms from tomograms of the *Chlamydomonas ida1* mutant, which we averaged in the previous work (Bui et al., 2012). In subaverages (averages of subtomograms, belonging to the same MTD), MTBDs from the adjacent MTD are visually detectable. We sorted these based on the positions of MTBDs from the adjacent MTD with respect to the ODAs on the MTD at the center of the box, and obtained three classes. The subaverages belonging to the same class were then further averaged.

ACCESSION NUMBERS

The density map of single particle analysis and the atomic model of fitted tubulins are deposited in the EM databank (EMD: 6312) and PDB (PDB: 3JAO), respectively.

SUPPLEMENTAL INFORMATION

Supplemental Information includes two figures and two videos and can be found with this article online at http://dx.doi.org/10.1016/j.str.2015.06.017.

AUTHOR CONTRIBUTIONS

A.M. did most of the specimen preparation and 3D reconstruction. J.M.O. did atomic model fitting and analysis. K.H.B. developed programs for 3D reconstruction. K.S. and Y.T. designed and prepared kinesin. T.I. designed the entire project and all the authors participated in the interpretation. A.M., J.M.O., K.H.B. and T.I. prepared the manuscript.

ACKNOWLEDGMENTS

We thank Dr. Andrea Prota, Prof. Michel Steinmetz (PSI), and Prof. Masahide Kikkawa (U. Tokyo) for helpful discussion, Prof. Timothy J. Richmond (ETH Zurich) for biochemical facilities, Dr. Roger Wepf and Peter Tittmann (EMEZ, ETH Zurich) for technical support on EM, and Dr. David F. Sargent (ETH Zurich) and Ms Katherine Marie Thieltges (PSI) for critical reading of the manuscript. This work was funded by grants from the Swiss National Science Foundation (NF31003A-125131/1 and NF3100A-144035), NCCBI, Swiss-Japan Cooperative Research Fund, and ETHIIRA (to T.I.). All commercial affiliations/conflicts of interest have been disclosed.

Received: November 25, 2014
Revised: May 26, 2015
Accepted: June 8, 2015
Published: July 23, 2015

REFERENCES

Alushin, G.M., Lander, G.C., Kellogg, E.H., Zhang, R., Baker, D., and Nogales, E. (2014). High-resolution microtubule structures reveal the structural transitions in αβ-tubulin upon GTP hydrolysis. Cell *157*, 1117–1129.

Amos, L., and Klug, A. (1974). Arrangement of subunits in flagellar microtubules. J. Cell Sci. *14*, 523–549.

Amos, L.A., and Löwe, J. (1999). How Taxol stabilises microtubule structure. Chem. Biol. *6*, R65–R69.

Bradford, M.M. (1976). A rapid and sensitive method for the quantitation of microgram quantities of protein utilizing the principle of protein-dye binding. Anal. Biochem. *72*, 248–254.

Bui, K.H., Sakakibara, H., Movassagh, T., Oiwa, K., and Ishikawa, T. (2008). Molecular architecture of inner dynein arms in situ in *Chlamydomonas reinhardtii* flagella. J. Cell Biol. *183*, 923–932.

Bui, K.H., Sakakibara, H., Movassagh, T., Oiwa, K., and Ishikawa, T. (2009). Asymmetry of inner dynein arms and inter-doublet links in *Chlamydomonas flagella*. J. Cell Biol. *186*, 437–446.

Bui, K.H., Yagi, T., Yamamoto, R., Kamiya, R., and Ishikawa, T. (2012). Polarity and asymmetry in the arrangement of dynein and related structures in the *Chlamydomonas axoneme*. J. Cell Biol. *198*, 913–925.

Cochran, J.C., Sindelar, C.V., Mulko, N.K., Collins, K.A., Kong, S.E., Hawley, R.S., and Kull, F.J. (2009). ATPase cycle of the nonmotile kinesin NOD allows microtubule end tracking and drives chromosome movement. Cell *136*, 110–122.

Conway, J.F., and Steven, A.C. (1999). Methods for reconstructing density maps of "single" particles from cryoelectron micrographs to subnanometer resolution. J. Struct. Biol. *128*, 106–118.

Frank, J., Radermacher, M., Penczek, P., Zhu, J., Li, Y., Ladjadj, M., and Leith, A. (1996). SPIDER and WEB: processing and visualization of images in 3D electron microscopy and related fields. J. Struct. Biol. *116*, 190–199.

Goodenough, U.W., and Heuser, J.E. (1985a). Outer and inner dynein arms of cilia and flagella. Cell *41*, 341–342.

Goodenough, U.W., and Heuser, J.E. (1985b). Substructure of inner dynein arms, radial spokes, and the central pair/projection complex of cilia and flagella. J. Cell Biol. *100*, 2008–2018.

Heuser, T., Raytchev, M., Krell, J., Porter, M.E., and Nicastro, D. (2009). The dynein regulatory complex is the nexin link and a major regulatory node in cilia and flagella. J. Cell Biol. *187*, 921–933.

Heuser, T., Barber, C.F., Lin, J., Krell, J., Rebesco, M., Porter, M.E., and Nicastro, D. (2012). Cryoelectron tomography reveals doublet-specific structures and unique interactions in the I1 dynein. Proc. Natl. Acad. Sci. USA *109*, E2067–E2076.

Kikkawa, M., Ishikawa, T., Nakata, T., Wakabayashi, T., and Hirokawa, N. (1994). Direct visualization of the microtubule lattice seam both in vitro and in vivo. J. Cell Biol. *127*, 1965–1971.

Kon, T., Oyama, T., Shimo-Kon, R., Imamula, K., Shima, T., Sutoh, K., and Kurisu, G. (2012). The 2.8 Å crystal structure of the dynein motor domain. Nature *484*, 345–350.

Konno, A., Setou, M., and Ikegami, K. (2012). Ciliary and flagellar structure and function—their regulations by posttranslational modifications of axonemal tubulin. Int. Rev. Cell Mol. Biol. *294*, 133–170.

Kremer, J.R., Mastronarde, D.N., and McIntosh, J.R. (1996). Computer visualization of three-dimensional image data using IMOD. J. Struct. Biol. *116*, 71–76.

Linck, R.W., and Stephens, R.E. (2007). Functional protofilament numbering of ciliary, flagellar, and centriolar microtubules. Cell Motil. Cytoskeleton *64*, 489–495.

Linck, R., Fu, X., Lin, J., Ouch, C., Schefter, A., Steffen, W., Warren, P., and Nicastro, D. (2014). Insights into the structure and function of ciliary and flagellar doublet microtubules: tektins, Ca^{2+}-binding proteins and stable protofilaments. J. Biol. Chem. *289*, 17427–17444.

Maheshwari, A., and Ishikawa, T. (2012). Heterogeneity of dynein structure implies coordinated suppression of dynein motor activity in the axoneme. J. Struct. Biol. *179*, 235–241.

Maurer, S.P., Fourniol, F.J., Bohner, G., Moores, C.A., and Surrey, T. (2012). EBs recognize a nucleotide-dependent structural cap at growing microtubule ends. Cell *149*, 371–382.

Mizuno, N., Narita, A., Kon, T., Sutoh, K., and Kikkawa, M. (2007). Three-dimensional structure of cytoplasmic dynein bound to microtubules. Proc. Natl. Acad. Sci. USA *104*, 20832–20837.

Movassagh, T., Bui, K.H., Sakakibara, H., Oiwa, K., and Ishikawa, T. (2010). Nucleotide-induced global conformational changes of flagellar dynein arms revealed by in situ analysis. Nat. Struct. Mol. Biol. *17*, 761–767.

Nicastro, D., Schwartz, C., Pierson, J., Gaudette, R., Porter, M.E., and McIntosh, J.R. (2006). The molecular architecture of axonemes revealed by cryoelectron tomography. Science *313*, 944–948.

Nicastro, D., Fu, X., Heuser, T., Tso, A., Porter, M.E., and Linck, R.W. (2011). Cryo-electron tomography reveals conserved features of doublet microtubules in flagella. Proc. Natl. Acad. Sci. USA *108*, E845–E853.

Nogales, E., Wolf, S.G., and Downing, K.H. (1998). Structure of the alpha beta tubulin dimer by electron crystallography. Nature *391*, 199–203.

Orias, E., Hamilton, E.P., and Orias, J.D. (2000). Tetrahymena as a laboratory organism: useful strains, cell culture, and cell line maintenance. Methods Cell Biol. *62*, 189–211.

Pazour, G.J., Agrin, N., Leszyk, J., and Witman, G.B. (2005). Proteomic analysis of a eukaryotic cilium. J. Cell Biol. *170*, 103–113.

Pettersen, E.F., Goddard, T.D., Huang, C.C., Couch, G.S., Greenblatt, D.M., Meng, E.C., and Ferrin, T.E. (2004). UCSF Chimera—a visualization system for exploratory research and analysis. J. Comput. Chem. *25*, 1605–1612.

Pigino, G., Bui, K.H., Maheshwari, A., Lupetti, P., Diener, D., and Ishikawa, T. (2011). Cryoelectron tomography of radial spokes in cilia and flagella. J. Cell Biol. *195*, 673–687.

Pigino, G., Maheshwari, A., Bui, K.H., Shingyoji, C., Kamimura, S., and Ishikawa, T. (2012). Comparative structural analysis of eukaryotic flagella and cilia from *Chlamydomonas*, *Tetrahymena*, and sea urchins. J. Struct. Biol. *178*, 199–206.

Porter, M.E. (1996). Axonemal dyneins: assembly, organization, and regulation. Curr. Opin. Cell Biol. *8*, 10–17.

Redwine, W.B., Hernández-López, R., Zou, S., Huang, J., Reck-Peterson, S.L., and Leschziner, A.E. (2012). Structural basis for microtubule binding and release by dynein. Science *337*, 1532–1536.

Rice, S., Lin, A.W., Safer, D., Hart, C.L., Naber, N., Carragher, B.O., Cain, S.M., Pechatnikova, E., Wilson-Kubalek, E.M., Whittaker, M., et al. (1999). A structural change in the kinesin motor protein that drives motility. Nature *402*, 778–784.

Rosenthal, P.B., and Henderson, R. (2003). Optimal determination of particle orientation, absolute hand, and contrast loss in single-particle electron cryomicroscopy. J. Mol. Biol. *333*, 721–745.

Sindelar, C.V., and Downing, K.H. (2010). An atomic-level mechanism for activation of the kinesin molecular motors. Proc. Natl. Acad. Sci. USA *107*, 4111–4116.

Song, Y.H., and Mandelkow, E. (1993). Recombinant kinesin motor domain binds to beta-tubulin and decorates microtubules with a B surface lattice. Proc. Natl. Acad. Sci. USA *90*, 1671–1675.

Song, Y.H., and Mandelkow, E. (1995). The anatomy of flagellar microtubules: polarity, seam, junctions, and lattice. J. Cell Biol. *128*, 81–94.

Sui, H., and Downing, K.H. (2006). Molecular architecture of axonemal microtubule doublets revealed by cryo-electron tomography. Nature *442*, 475–478.

Witman, G.B. (1986). Isolation of *Chlamydomonas flagella* and flagellar axonemes. Methods Enzymol. *134*, 280–290.

Yanagisawa, H., Mathis, G., Oda, T., Hirono, M., Richey, E.A., Ishikawa, H., Marshall, W.F., Kikkawa, M., and Qin, H. (2014). FAP20 is an inner junction protein of doublet microtubules essential for both the planar asymmetrical waveform and stability of flagella in *Chlamydomonas*. Mol. Biol. Cell *25*, 1472–1483.